Seasonal variations of aerosol optical properties, vertical distribution and associated radiative effects in the Yangtze Delta region of China

Jianjun Liu,[1,2] Youfei Zheng,[1] Zhanqing Li,[2,3,4] Connor Flynn,[5] and Maureen Cribb[2]

[1] Four years of columnar aerosol optical properties and a one-year vertical profiles of aerosol particle extinction coefficient at 527 nm are analyzed at Taihu in the central Yangtze River Delta region in eastern China. Seasonal variations of aerosol optical properties, vertical distribution, and influence on shortwave radiation and heating rates were investigated. Multiyear variations of aerosol optical depths (AOD), Ångstrom exponents, single scattering albedo (SSA) and asymmetry factor (ASY) are analyzed, together with the vertical profile of aerosol extinction. AOD is largest in summer and smallest in winter. SSAs exhibit weak seasonal variation with the smallest values occurring during winter and the largest during summer. The vast majority of aerosol particles are below 2 km, and about 62%, 67%, 67% and 83% are confined to below 1 km in spring, summer, autumn and winter, respectively. Five-day back trajectory analyses show that the some aerosols aloft are traced back to northern/northwestern China, as far as Mongolia and Siberia, in spring, autumn and winter. The presence of dust aerosols were identified based on the linear depolarization measurements together with other information (i.e., back trajectory, precipitation, aerosol index). Dust strongly impacts the vertical particle distribution in spring and autumn, with much smaller effects in winter. The annual mean aerosol direct shortwave radiative forcing (efficiency) at the bottom, top and within the atmosphere are -34.8 ± 9.1 (-54.4 ± 5.3), -8.2 ± 4.8 (-13.1 ± 1.5) and 26.7 ± 9.4 (41.3 ± 4.6) W/m^2 (Wm^{-2} τ^{-1}), respectively. The mean reduction in direct and diffuse radiation reaching surface amount to 109.2 ± 49.4 and 66.8 ± 33.3 W/m^2, respectively. Aerosols significantly alter the vertical profile of solar heating, with great implications for atmospheric stability and dynamics within the lower troposphere.

1. Introduction

[2] It is well known that atmospheric aerosol particles play an important role in the climate system and the hydrological cycle because they absorb and scatter solar radiation, serve as nuclei in the formation of cloud particles and participate in many chemical and photochemical reactions [*Twomey*, 1977; *Ackerman et al.*, 2000; *Rosenfeld et al.*, 2001, 2008; *Kaufman et al.*, 2005; *Forster et al.*, 2007; *Clarke and Kapustin*, 2010; *Engling and Gelencser*, 2010]. Significant long-term impacts on cloud vertical development and rain frequency and rate have been identified, implying larger roles that aerosols play in modulating earth's water and energy cycle than previously thought [*Li et al.*, 2011a].

[3] Knowledge of optical properties, such as the aerosol optical depth (AOD), the single scattering albedo (SSA), the asymmetry factor (ASY), and their vertical distributions is critical for estimating the effect of aerosol particles on radiative forcing and their associated impacts on climate. Studies showed that when using column-integrated AOD and column-mean SSA and ASY in calculations of aerosol direct radiative forcing (ADRF), the vertical distribution of the aerosol extinction coefficient had very little impact on ADRF at the top-of-the-atmosphere (TOA) and surface but

---

[1]Jiangsu Key Laboratory of Atmospheric Environment Monitoring and Pollution Control, Nanjing University of Information Science and Technology, Nanjing, China.
[2]Department of Atmospheric and Oceanic Science and Earth System Science Interdisciplinary Center, University of Maryland, College Park, Maryland, USA.
[3]State Key Laboratory of Earth Surface Processes and Resource Ecology, GCESS, Beijing Normal University, Beijing, China.
[4]State Laboratory of Earth Surface Process and Resource Ecology, College of Global Change and Earth System Science, Beijing Normal University, Beijing, China.
[5]Climate Physics Group, Pacific Northwest National Laboratory, Richland, Washington, USA.

significantly changed the vertical distribution of the heating rate [*Chou et al.*, 2006; *Johnson et al.*, 2008; *Guan et al.*, 2010]. This modifies the stability of the atmosphere, which affects convective and turbulent motions [*McFarquhar and Wang*, 2006; *Ramanathan et al.*, 2007], and can even affect regional climate circulation [*Ramanathan et al.*, 2001b]. To date, however, knowledge of aerosol particle properties and their spatial and temporal variations, as well as their vertical structure, is still very poor, which results in considerable uncertainties in the understanding of complex climate effects [*Forster et al.*, 2007].

[4] Recently, aerosols over East Asia, especially over eastern China, have attracted considerable attention because of their high surface concentrations and the coexistence of dust, industrial pollutants and biomass burning aerosols [*Lau et al.*, 2008]. Recent international aerosol-focused experiments have been conducted off the main continent of East Asia, mostly along the eastern shore region of Asia including Japan and Korea [*Huebert et al.*, 2003; *Nakajima et al.*, 2003, 2007]. Since 2004, two major aerosol experiments were conducted in mainland China: the East Asian Study of Tropospheric Aerosols: An International Regional Experiment (EAST-AIRE) [*Li et al.*, 2007] and the East Asian Study of Tropospheric Aerosols and Impact on Regional Climate (EAST-AIRC) [*Li et al.*, 2011b]. In the latter experiment, the U.S. Department of Energy's Atmospheric Radiation Measurement (ARM) Mobile Facility (AMF) was deployed in China from June 2008 to May 2009. Together with instruments provided by collaborating institutions, intensive observations were made at four sites representing distinct climate and environmental regimes across China [*Li et al.*, 2011b]. As a site for both field experiments, the Taihu station (31.7N, 120.4E, 10 m above sea level) was established in 2005 along the shores of Lake Taihu, which is in the heart of the Yangtze River Delta region surrounded by several large cities: Shanghai (31.2N, 121.5E) to the east, Nanjing (32.0N,118.8E) to the west and Hangzhou (30.3N, 120.2E) to the south.

[5] Since 2005, a CIMEL sunphotometer, broadband radiometers, a total sky imager and a multifilter rotating shadowband radiometer (MFRSR) were operated at the Taihu site to continuously measure aerosol particle optical properties and surface radiation as a part of the EAST-AIRE. In May 2008, a depolarization-sensitive micropulse lidar (MPL) and a microwave radiometer were added to the instrument suite already in operation at the site [*Li et al.*, 2011b]. This was the first time that long-term ground-based measurements of aerosol optical properties and their vertical distribution from the MPL were collected over this highly populated area in China. Evaluation of the vertical distribution of aerosols can now be made in this region, where anthropogenic activities lead to exceptionally high aerosol loading [*Li et al.*, 2007] and significant thermal perturbation created by diabatic heating and direct radiative forcing [*Xia et al.*, 2007].

[6] This paper presents results from the analysis of aerosol particle optical properties and associated radiation measurement collected from 2006 to 2009 at Taihu, and a full year of MPL data collected during the 2008–2009 field campaign. Brief descriptions of measurements made and methods used in the analyses are given in Section 2. Section 3 is a summary of the seasonal characteristics of

aerosol particle optical properties, their vertical distribution and their shortwave direct radiative effects. The influence of dust aerosols on the seasonal variations of aerosol properties and their radiative effects are also discussed in this section. Conclusions are given in Section 4.

2. Measurements and Methodology

2.1. Aerosol Optical Properties

[7] The Cimel sunphotometer, the standard instrument used in the NASA Aerosol Robotic Network (AERONET) [*Holben et al.*, 1998], measures direct solar and sky radiance at discrete wavelengths. Inversion retrieval methods were applied to determine AOD, SSA, ASY and the aerosol particle size distribution [*Dubovik et al.*, 2000]. The uncertainty in AOD is 0.01–0.02 and SSA for high AOD (>0.4 at 440 nm) and for large solar zenith angles (>50°) has an accuracy of ∼0.03 [*Dubovik et al.*, 2000]. Measurements at 940 nm are used to derive the water vapor column amount. Here, we use the Level 2.0 version of AERONET data (calibrated and screened for clouds) to estimate seasonal patterns of columnar optical properties. The version 2 retrievals of SSA and ASY for AOD at 440 nm larger than 0.4 and for solar zenith angles larger than 50° are used in the study. Level 1.5 AOD data is used as a constraint for MPL retrievals because of the smaller amount of Level 2.0 data available. Presence of thin cirrus clouds may not be identified which can lead to a bias of 0.03–0.08 in AOD [*Huang et al.*, 2011; *Chew et al.*, 2011].

[8] No AERONET retrievals were made at the site in July and August 2008, so AOD retrievals from the MFRSR were used instead. *Lee et al.* [2010] show that MFRSR AOD retrievals are in general agreement with AERONET retrievals of AOD at Taihu. The MFRSR is a seven-channel pyranometer with a rotating shadow band that measures total and diffuse solar broadband irradiances at 415, 500, 610, 673, 870, and 940 nm at 1-min intervals [*Harrison and Michalsky*, 1994]. The method proposed by *Lee et al.* [2010] was used to calibrate the instrument under hazy and highly variable aerosol scenes, and the method of *Alexandrov et al.* [2008] was used to retrieve AOD. The root-mean square difference between measurements calibrated using the method of *Lee et al.* [2010] and that of the standard Langley plot technique is 6% [*Lee et al.*, 2010], which translates to an accuracy of ∼0.03 and is comparable with the standard accuracy of well calibrated Sun photometers (∼0.026) using the Langley plot technique [*Schmid et al.*, 1999]. In addition to the calibration error, the typical retrieval accuracy is ∼0.01 [*Alexandrov et al.*, 2008]. Cloud screening is based on the local variability of optical depth derived from direct-beam measurements at 870 nm [*Alexandrov et al.*, 2004].

2.2. Aerosol Vertical Distribution

[9] The MPL installed at Taihu is based on an eye safe and compact solid state lidar originally developed at the NASA Goddard Space Flight Center and manufactured by the Sigma Space Corporation. The instrument used here has been augmented with polarization sensitivity, as described by *Flynn et al.* [2007]. The instrument operates at 527 nm and the laser pulse duration is about 10 ns with a pulse repetition rate of 2500 Hz. Signals are measured with
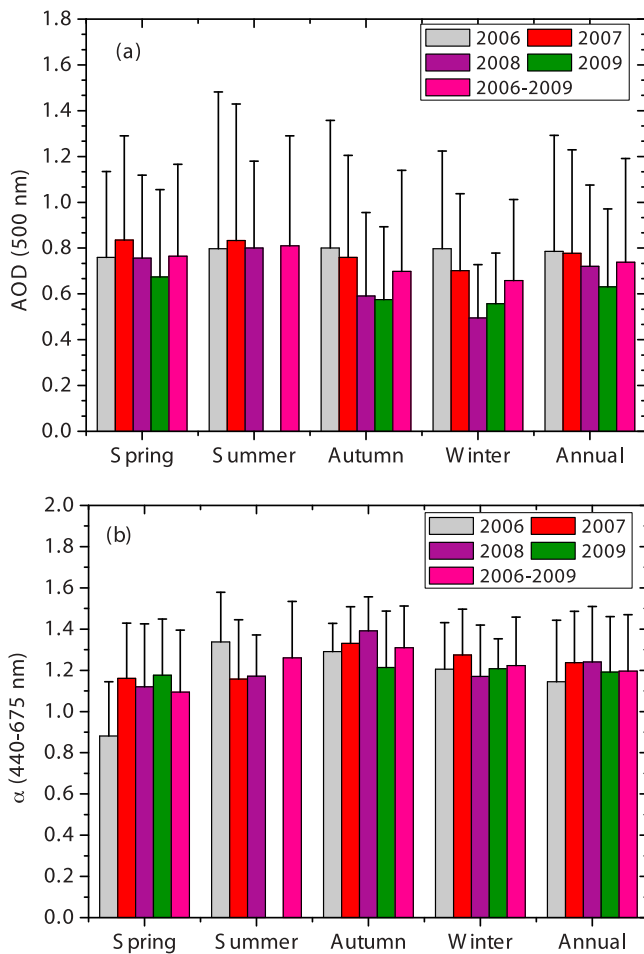
Figure 1. Seasonal and annual mean (a) AOD (500 nm) and (b) α (440–675 nm) with corresponding standard deviations. Data are from 2006 to 2009 at Taihu.

vertical resolution set at 30 m for this study. The MPL receiver measures many low-energy pulses in a short time enabling it to achieve a good signal-to-noise ratio [*Welton et al.*, 2002; *Campbell et al.*, 2002]. It is capable of detecting cloud and aerosol structures up to 20 km in altitude during the day [*Campbell et al.*, 2008]. The instrument is designed for unattended data acquisition. *Spinhirne* [1993] and *Campbell et al.* [2002] provide more detailed descriptions of the MPL.

[10] The backscattered radiation detected by a single-channel elastic-scattering lidar is described by the following equation:

$$P(r) = O_c(r)CE\frac{\beta(r)}{r^2}\exp\left[-2\int_0^r \sigma(z)dz\right] + N_b + A(r), \quad (1)$$

where r is the range and $\beta(r)$ and $\sigma(r)$ are the combined aerosol and molecular backscattering and extinction coefficients at range r. Other parameters in the equation are the lidar calibration constant (C), the laser pulse energy (E), and the background noise (N_b). Instrument effects include the overlap function (O(r)) and the afterpulse, or receiver "crosstalk" function, (A(r)). Background noise and instrument

effects must be reconciled before processing the raw signal. Details describing this process are given by *Campbell et al.* [2002] and *Welton et al.* [2002]. After all signal corrections are made, the normalized relative backscatter, $P_{NRB}(r)$, or NRB, is obtained as

$$P_{NRB}(r) = C\beta(r)\exp\left[-2\int_0^r \sigma(z)dz\right], \quad (2)$$

where C is solved though a technique commonly constrained by co-located the AERONET AOD and at a range where molecular scattering is identified above the surface detected aerosol layer and is cloud-free [*Welton et al.*, 2002]. The method of *Campbell et al.* [2008] is used to estimate the top height of the surface-detected aerosol layer and cloud screening follows the method of *Wang and Sassen* [2001]. We used the method developed by *Fernald* [1984], and adopted for MPL retrievals, to solve for layer average extinction-backscatter ratios (LR) and aerosol extinction coefficient profiles [*Welton et al.*, 2000, 2002]. Details concerning the generation of polarization-sensitive lidar measurements and the calculation of the linear depolarization ratio, δ_{linear}, are given by *Flynn et al.* [2007].

3. Results

[11] Annual and seasonal variations in aerosol particle optical properties were investigated using four years of passive ground-based measurements (2006–2009). From retrievals made during this period, 12,644 instantaneous retrievals of AOD and α and 1,237 instantaneous retrievals of SSA and ASY were available for analysis. Lidar retrievals from June 2008 to May 2009 were used to study the vertical distribution of aerosols and to estimate their effects on the radiation budget. Seasons are defined as: March–May (spring), June–August (summer), September–November (autumn) and December–February (winter).

3.1. Optical Properties

[12] Figure 1 shows the annual and seasonal variations of mean AOD at 500 nm and α at 440–675 nm with their corresponding standard deviations for the period of 2006–2009. The annual mean AOD for each year was 0.79 ± 0.51, 0.78 ± 0.48, 0.72 ± 0.40 and 0.63 ± 0.34, respectively. Standard deviations are greater than 50% of the mean, indicating that AODs varied greatly throughout the years. Figure 1 also reveals a gradual reduction in annual mean AOD of about -3.4%, -8.4% and -9.3% per year from 2006 to 2009 during the spring, autumn and winter seasons, respectively. The decrease in AOD in autumn is statistically significant with a confidence level of 0.1 (P = 0.1), but is not in other seasons. A similar analysis for the summer season was not done because of a lack of AOD retrievals during the summer of 2009.

[13] In terms of seasonal variation, maxima in overall mean AOD occurred in spring and summer (0.76 ± 0.40 and 0.81 ± 0.48, respectively). In spring, dust aerosols are transported out of northwest China and can increase aerosol loading over Taihu [*Tsai et al.*, 2008; *J. Liu et al.*, 2011]. This is illustrated in Figure 2, which shows the aerosol particle size distribution for each season. Relatively high concentrations of coarse-mode particles are present during
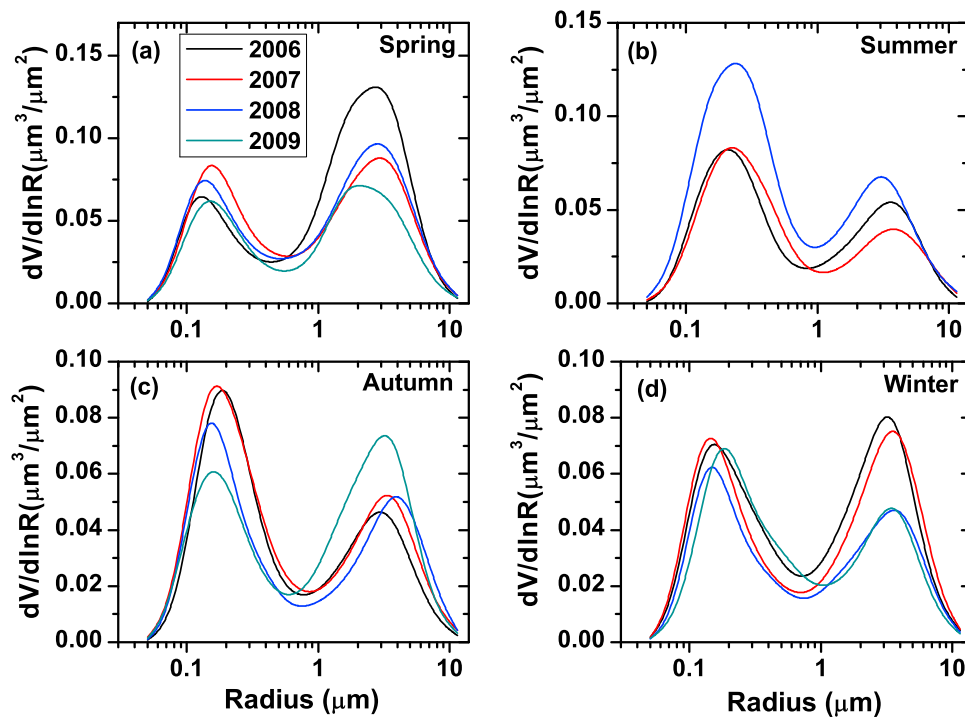
Figure 2. Seasonal mean aerosol particle size distributions for (a) spring (March–May), (b) summer (June–August), (c) autumn (September–November) and (d) winter (December–February). Data are from 2006 to 2009 at Taihu.

spring (Figure 2a). In summer, high values of AOD occur because of higher relative humidity during this season inducing deliquescence and particle growth and an increase in fine-mode anthropogenic aerosols (see Figure 2b) due to the build-up of local pollution resulting from the presence of a persistent and stagnant synoptic meteorological system over the Asian continent [*Kim et al.*, 2007]. During autumn and winter, relatively strong winds to the lower Yangtze River Delta region, diluting pollutants and lowers the aerosol loading [*Pan et al.*, 2010]. Frequency distributions of AOD shown in Figure 3a, illustrate the broad range of values observed from 2006 to 2009, and the high aerosol loading prevalent year-round over the region. Accumulated frequencies of AOD in the range less than 0.5, 0.5 to 1.0 and greater than 1.0 are about 34.9%, 45.2% and 19.9%, respectively. Only 2.5% of all values of AOD are less than 0.2.

[14] The Ångstrom exponent, which varies with particle size, is derived from AOD retrievals made at 440 nm and 675 nm. Figure 1b shows that the annual mean α was 1.14 ± 0.30, 1.23 ± 0.25, 1.24 ± 0.27 and 1.19 ± 0.27 from 2006 to 2009, respectively. Seasonal mean α during the study period was 1.09 ± 0.30, 1.26 ± 0.27, 1.31 ± 0.20, and 1.22 ± 0.23 for spring, summer, autumn and winter, respectively. The magnitude of α was smallest in spring and largest in autumn. This variation may reflect changes in the origin of aerosol particles and transport routes [*Léon et al.*, 2009], although these values fall well within the range of the standard deviations. An influx of dust particles from the northern/northwest regions of China, carried in by winds associated with the Asian monsoon and continental anticyclones [*Tsai et al.*, 2008; *J. Liu et al.*, 2011], is the likely cause for the relatively low springtime minimum. It is worth

noting that aerosol particles can affect the Asian monsoon circulation as well [*Niu et al.*, 2010]. Figure 3b shows that α ranges from 0.1 to 1.9 with a peak in the distribution between 1.2 and 1.5. This illustrates that the aerosol particle type in this region is highly variable. The accumulated frequencies of α less than 1.0 and greater than 1.0 are about 20.6%, and 79.4%, respectively. Only 1.6% of all values of α was less than 0.5 and occurred in spring when dust events occasionally impact the site.

[15] Table 1 summarizes annual and seasonal variation in mean SSA and ASY at 675 nm, as well as annual minimum and maximum values of each quantity. From 2006 to 2009, annual mean values of SSA were 0.921 ± 0.032, 0.906 ± 0.038, 0.907 ± 0.033 and 0.922 ± 0.024, respectively. The seasonal mean SSA over the period of 2006–2009 was 0.922 ± 0.028, 0.925 ± 0.042, 0.917 ± 0.031 and 0.892 ± 0.034 in spring, summer, autumn and winter, respectively. Low values of SSA in winter are mainly due to the dominance of absorbing urban aerosol particles prevalent during the heating period. Figure 3c shows that the majority of SSA values (84%) fall in the range of 0.85 to 0.95. The wide range of SSA values (0.726–0.992 in terms of instantaneous values) illustrates there were quite different aerosol particle types and optical characteristics at this location.

[16] Magnitudes of ASY were relatively constant from 2006 to 2009 (see Table 1). Annual mean values were 0.658 ± 0.029, 0.656 ± 0.039, 0.649 ± 0.039 and 0.657 ± 0.028 in 2006, 2007, 2008 and 2009, respectively. Seasonal mean values of ASY for the entire period were 0.655 ± 0.034, 0.681 ± 0.042, 0.649 ± 0.036, 0.652 ± 0.034 in spring, summer, autumn and winter, respectively. Nearly 84% of all values of ASY fell in the range of 0.6–0.7 (Figure 3d). Hygroscopic growth may explain why SSA and ASY are
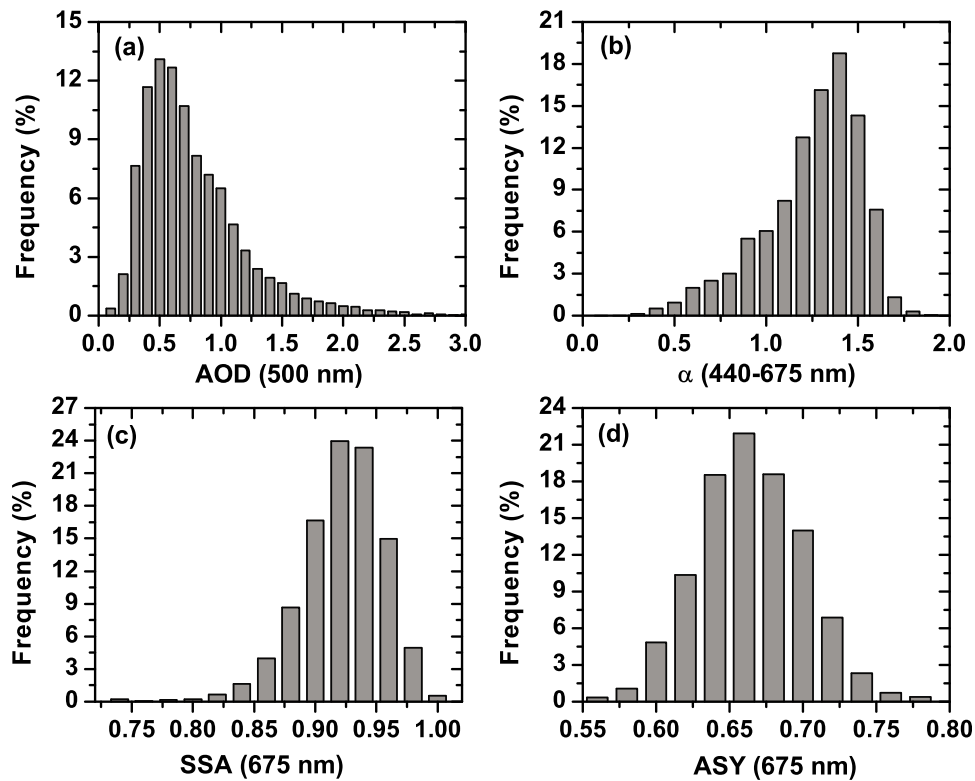
Figure 3. Histograms of (a) AOD (500 nm), (b) α (440–675 nm), (c) SSA (675 nm) and (d) ASY (675 nm). Data are from 2006 to 2009 at Taihu.

largest during the summer season. For a fixed composition, hygroscopic growth under humid conditions can lead to an increase in particle size (therefore increasing ASY) and cause enhanced forward scattering (therefore increasing SSA) [*Jeong et al.*, 2007; *Xia et al.*, 2007].

[17] Figure 4 presents the seasonal mean values of spectral aerosol SSA and ASY at 440, 675, 870 and 1020 nm with corresponding standard deviations at Tahihu during 2006–2009. The SSA showed a relatively weak dependence on wavelength with a slight increase from 440 to 675 nm and almost invariable over 675–1020 nm. The annual mean SSAs at the four wavelengths are 0.892 ± 0.038, 0.912 ± 0.035, 0.909 ± 0.041 and 0.908 ± 0.046, respectively. The

seasonal mean ASY showed a decreasing trend with wavelength in summer, autumn and winter. But in spring, ASY decreased over 440–870 nm and slightly increased over 870–1020 nm, which is related to the dust activity in spring [*X. Yu et al.*, 2009]. The annual mean ASYs at the four wavelengths are 0.720 ± 0.026, 0.655 ± 0.036, 0.629 ± 0.040 and 0.626 ± 0.043, respectively.

3.2. Vertical Distribution of Aerosols

3.2.1. Seasonal Characteristics

[18] From June 2008 to May 2009, 131 daily mean aerosol extinction profiles were analyzed to derive the seasonal mean vertical profiles. Of these daily profiles, 49 were in spring,

Table 1. Seasonal Mean, Minimum, Maximum and Annual Mean SSA and ASY at 675 nm Retrieved From AERONET Measurements Taken at Taihu From 2006 to 2009[a]

Year	Spring	Summer	Autumn	Winter	Min	Max	Annual
			SSA (675 nm)				
2006	0.934 ± 0.021	0.939 ± 0.034	0.936 ± 0.027	0.896 ± 0.027	0.838	0.982	0.921 ± 0.032
2007	0.921 ± 0.025	0.908 ± 0.047	0.911 ± 0.031	0.888 ± 0.042	0.726	0.992	0.906 ± 0.038
2008	0.916 ± 0.033	0.947 ± 0.019	0.900 ± 0.031	0.893 ± 0.027	0.804	0.978	0.907 ± 0.033
2009	0.918 ± 0.027	n/a	0.931 ± 0.017	0.915 ± 0.026	0.810	0.975	0.922 ± 0.024
all	0.922 ± 0.028	0.925 ± 0.042	0.917 ± 0.031	0.892 ± 0.034			0.912 ± 0.035
			ASY (675 nm)				
2006	0.664 ± 0.022	0.664 ± 0.033	0.645 ± 0.026	0.653 ± 0.034	0.584	0.744	0.658 ± 0.029
2007	0.654 ± 0.036	0.697 ± 0.041	0.650 ± 0.037	0.652 ± 0.036	0.565	0.775	0.656 ± 0.039
2008	0.652 ± 0.039	0.670 ± 0.046	0.634 ± 0.045	0.648 ± 0.032	0.555	0.755	0.649 ± 0.039
2009	0.651 ± 0.030	n/a	0.665 ± 0.023	0.679 ± 0.023	0.594	0.721	0.657 ± 0.028
all	0.655 ± 0.034	0.681 ± 0.042	0.649 ± 0.036	0.652 ± 0.034			0.655 ± 0.036

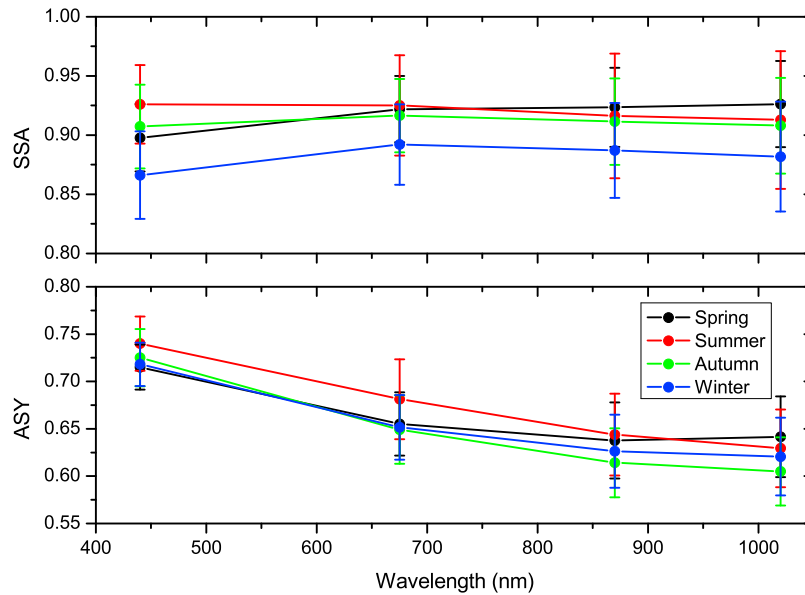[a]Abbreviation: n/a, data available; Min, minimum; Max, maximum.

Figure 4. Seasonal means of the spectral (top) SSA and (bottom) ASY at 440, 675, 870 and 1020 nm with corresponding standard deviations. Data are from 2006 to 2009 at Taihu.

24 in summer, 28 in autumn and 30 in winter. Figure 5 shows seasonal (blue lines) and annual (red lines) mean aerosol particle extinction coefficient profiles at 527 nm for all seasons. Horizontal lines represent standard deviations of the seasonal mean. The uncertainty in MPL retrievals is very high in the first 300 m from the surface due to instability of the overlap function [*Campbell et al.*, 2002], so vertical profiles shown in Figure 5 begin at 300 m. The overlap function was evaluated in a qualitative sense by comparing profiles of attenuated backscatter (which require overlap

correction) with simultaneous profiles of depolarization ratio (which are intrinsically immune to overlap effects). Under well-mixed conditions, profiles of these two quantities both displayed good vertical uniformity even to within ∼100 m suggesting that the overlap correction is quite adequate for aerosol retrievals.

[19] The highest extinction occurs below 2 km, gradually decreasing with height. The maximum value for annual mean extinction was about 0.28 km^{-1}, which was located near the surface. The maximum values of aerosol extinction
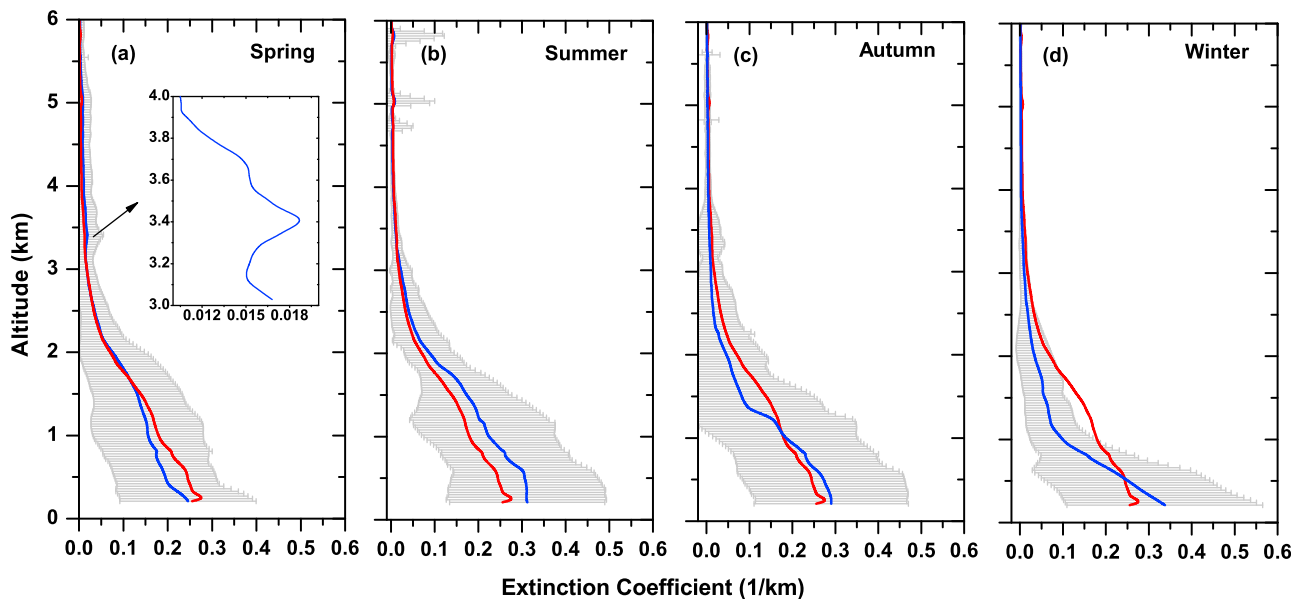

Figure 5. Seasonal (blue lines) and annual (red lines) mean aerosol particle extinction coefficient profiles at 527 nm for (a) spring, (b) summer, (c) autumn and (d) winter from June 2008 to May 2009 at Taihu. Horizontal lines represent standard deviations. A magnification of the profile from 3 to 4 km is shown in Figure 5a.
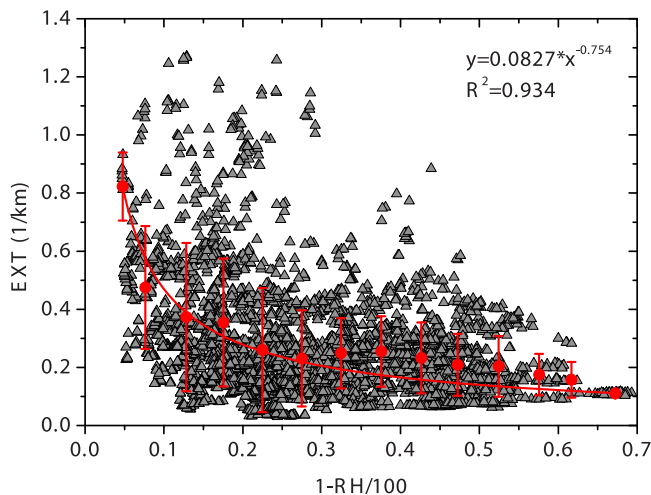
Figure 6. Near-surface extinction coefficients at 527 nm as a function of (1- RH/100).

were about 0.24 km^{-1}, 0.29 km^{-1} and 0.32 km^{-1} (located ~0.3 km) in spring, autumn and winter, respectively; in summer, the maximum value of aerosol extinction was 0.31 km^{-1}, which was located at 0.36 km. A close-up of the springtime profile from 3 to 4 km (see inset of Figure 5a) shows that the extinction coefficient reaches a maximum value of approximately 0.019 km^{-1}. This elevated layer is attributed to Asian dust transport [*J. Liu et al.*, 2011]. Studies of aerosol particle vertical distributions over the Korean Peninsula and over Hong Kong [*Kim et al.*, 2007; *He et al.*, 2008] also show that elevated dust aerosol layers are found during this springtime. Compared to the annual mean, the extinction coefficient during spring was smaller below 1.5 km, but slightly larger above 1.5 km indicating that the aerosol loading was enhanced above the boundary layer. Aerosol particle extinction coefficients were greatest during the summer at most altitudes. We attribute this to particle lifting and convective instabilities during the hot summer months [*Wang et al.*, 2010]. In fall, profile values regress to the annual mean, decreasing gradually from 0.29 km^{-1} to 0.15 km^{-1} from the surface to 1.2 km then decreasing to 0.01 km^{-1} from 1.2 km to 3.0 km. Of all seasons, aerosol particle extinction was highest within the first 1 km in winter, where it decreased from 0.32 km^{-1} at the surface to 0.1 km^{-1} at the 1-km level. Winter conditions in the region are climatologically stable from 500 to 700 m above ground level [*He et al.*, 2008], confining aerosols within the lowest level of the atmosphere.

[20] Humidity is an important factor influencing how extinction coefficients change with the seasons, and is likely responsible for the occurrence of large extinction coefficients at low altitudes. Heavy concentrations of pollutants present near the surface in this region are generally hygroscopic. Figure 6 shows near-surface (~0.3 km altitude) extinction coefficients derived from the MPL as a function of relative humidity (RH: expressed as [1-RH/100]). RH was measured with the Vaisala WXT510 weather transmitter installed at Taihu. The exponential relationship exhibited in Figure 6 shows that the magnitudes of the extinction

coefficient increase as RH increases (R^2 = 0.933). *Xu et al.* [2002] also reported that condensed water typically contributes ~40% to the light scattering budget in eastern Asia.

[21] Figure 7 is a bar graph of seasonal and annual mean fractional AOD at 527 nm over the Taihu site partitioned below 1 km, between 1 and 3 km and above 3 km, based upon aerosol extinction profiles measured by the MPL from June 2008 to May 2009. The proportion of aerosol loading below 1 km in spring, summer, autumn, winter and overall is 62%, 67%, 67%, 83%, and greater than 70% of the total column loading, respectively. An interesting feature is that a small amount of aerosol particle loading is present year-round above 3 km.

3.2.2. Source Analysis at Different Altitudes

[22] Surface wind measurements taken at Taihu and corresponding 5-day air mass back trajectories ending at the site at 0.5-km and 2.5-km above ground level (AGL) were used to estimate the sources of aerosol particles arriving at Taihu at different altitudes. Surface wind speeds and directions were measured using an ultrasonic wind sensor on the Vaisala WXT510 weather transmitter installed at the site. The data were matched with MPL-derived extinction coefficients. The Hybrid Single Particle Lagrangian Integrated Trajectory (HYSPLIT) model (R. R. Draxler and G. D. Rolph, HYSPLIT (HYbrid Single-Particle Lagrangian Integrated Trajectory) Model, 2010, access via NOAA ARL READY Website (http://ready.arl.noaa.gov/HYSPLIT.php)) was used together with the Global Data Assimilation System (GDAS1) meteorological database [*Kalnay et al.*, 1996] as input to calculate corresponding air mass back trajectories. Figure 8a shows the wind rose diagram for the study period. The distribution of near-surface aerosol extinction coefficients in relation to wind direction and speed are given in Figure 8b. The wind rose diagram indicates that winds were mostly from the east with speeds less than 3 m/s, suggesting that the source of particles near the surface are probably related to local processes. Surface extinction coefficients generally range from 0.2 to 0.4 km^{-1} regardless of the wind direction (Figure 8b). Also, high surface extinction
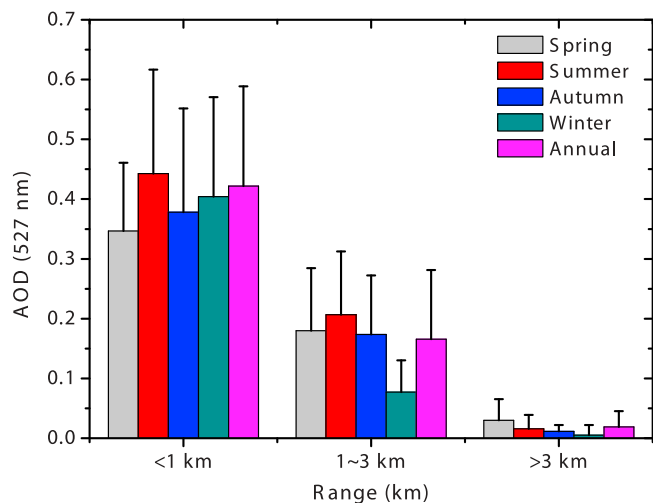

Figure 7. Seasonal and annual mean fractional AOD (at 527 nm) over the Taihu site partitioned below 1 km, between 1 and 3 km and above 3 km.
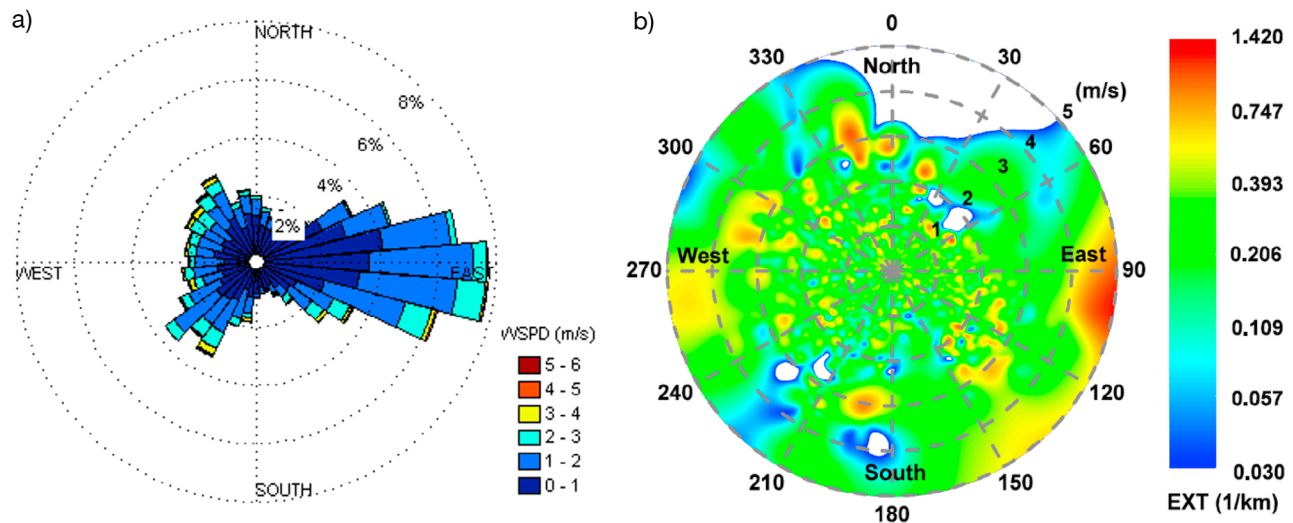
Figure 8. (a) Wind rose diagram based on measurements taken from 2008 to 2009 and (b) a shaded radial graph showing near-surface aerosol particle extinction coefficients at 527 nm as a function of wind direction and speed.

coefficients are associated with relatively strong winds (speeds greater than 4 m/s) from the east, suggesting that the regional transport of locally generated aerosol particles from densely populated areas east of the site contributes to surface aerosol loading at Taihu.

[23] Five-day air mass back trajectories ending at 0.5-km and 2.5-km AGL over Taihu for each season are shown in Figures 9 and 10, respectively. These two altitudes were chosen to represent the near-surface layer and upper layer [*Wang et al.*, 2010]. Eight groups of back trajectories were identified according to their origins and transport routes taken to reach the site, and are outlined in Table 2. Group 1 and group 2 may originate from the Mongolia or Siberia or northern China region. Group1 passes over the heavily polluted interior and coastal areas of northern China and group 2 passes the East China Sea before reaching the site. Group 3 originates from clean marine atmosphere and reaches the site over densely populated eastern/southeastern regions of China. The air masses, coming from northwestern China and passing through the Hexi region and Loess Plateau, are classified as group 4. Groups 5 and 6 originate southeast land and southwestern part of China, and passes over the southeast coast of China and southwestern of China, respectively. The group 7 comes from Indochina region and group 8 is defined as local air mass, respectively.

[24] Trajectories at the 0.5-km level over Taihu for all seasons except summer illustrate that for the most part, air masses most commonly originated from the north. In spring, most trajectories can be traced back as far north as Mongolia and Siberia, passing over the heavily polluted interior and coastal areas of northern China before reaching Taihu (Group 1). A smaller group of trajectories also pass over the interior of northern China, then over the East China Sea before reaching Taihu (Group 2). Some trajectories originate from the clean marine atmosphere and then move toward the densely populated eastern/southeastern regions of China before reaching Taihu (Group 3). For back trajectories ending at the 2.5-km level over Taihu (Figure 10), air masses generally originate from the north and follow the same paths

in the free troposphere as those of Groups 1 and 2. Some originate from northwestern China and travel across the Hexi corridor and the Loess Plateau, the so-called "dust corridor" [*Liu et al.*, 2008], to Taihu (Group 4). Another group transports air laden with anthropogenic pollutants from along the southeast coast of China toward Taihu (Group 5). Clean air masses originating from the less polluted southwestern part of China are also seen (Group 6).

[25] About two-thirds of the back trajectories ending at the 0.5-km level over Taihu during the summer are characterized as Group 3 (Figure 9 and Table 2). The remaining one-third either originate in northern China and Mongolia, traveling over the north/northeastern part of the country and the East China Sea, or originate in Indochina and travel northward over southeastern China (Group 7) before reaching Taihu. This latter air mass likely carries a mixture of biomass burning aerosols from Indochina and anthropogenic aerosols from southeastern China to the site [*Wang et al.*, 2010]. Trajectories arriving at Taihu at the 2.5-km level in summertime (Figure 10b) generally fall into the Group 1/ Group 2 categories (i.e., from the north/northwestern part of China), and Group 5/Group 6 categories (i.e., southeast/ southwest directions).

[26] In autumn, about three-quarters of the trajectories at the 0.5-km level were tracked back to Mongolia and Siberia, traveling over the interior portion of northern China and the East China Sea. Additionally, some trajectories are local (Group 8), indicating that nearby emissions may play an important role in aerosol loading at the site during this season. Back trajectories arriving at the 2.5-km level show that about two-thirds tracked to Mongolian and Siberian regions and northwestern China and follow Group 1/Group 2 pathways to Taihu. A small number of air masses originate from southeastern and southwestern China (Group 5/Group 6 pathways). It should be pointed out that while different origins were identified, the physical and chemical properties of aerosol particles may be altered en-route due to local surface emissions.
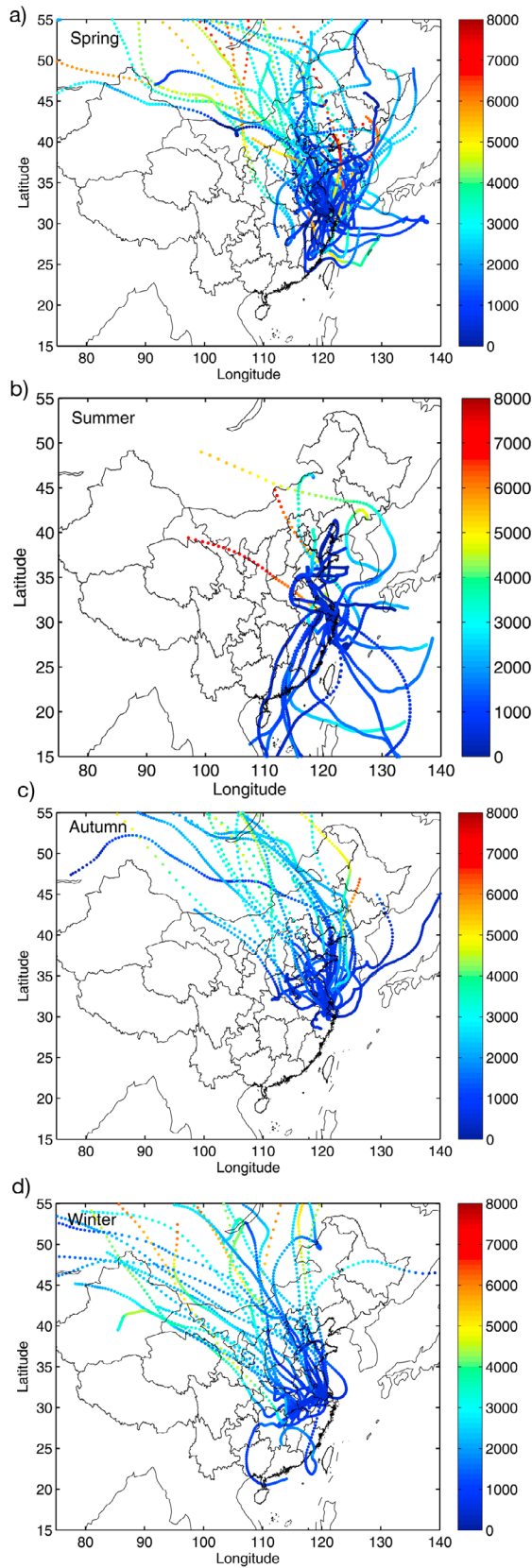
Figure 9. Five-day HYSPLIT back trajectories ending at 0.5-km AGL for days when vertical extinction profiles were available in (a) spring, (b) summer, (c) autumn and (d) winter. The color scale represents trajectory altitudes (AGL, unit: m).
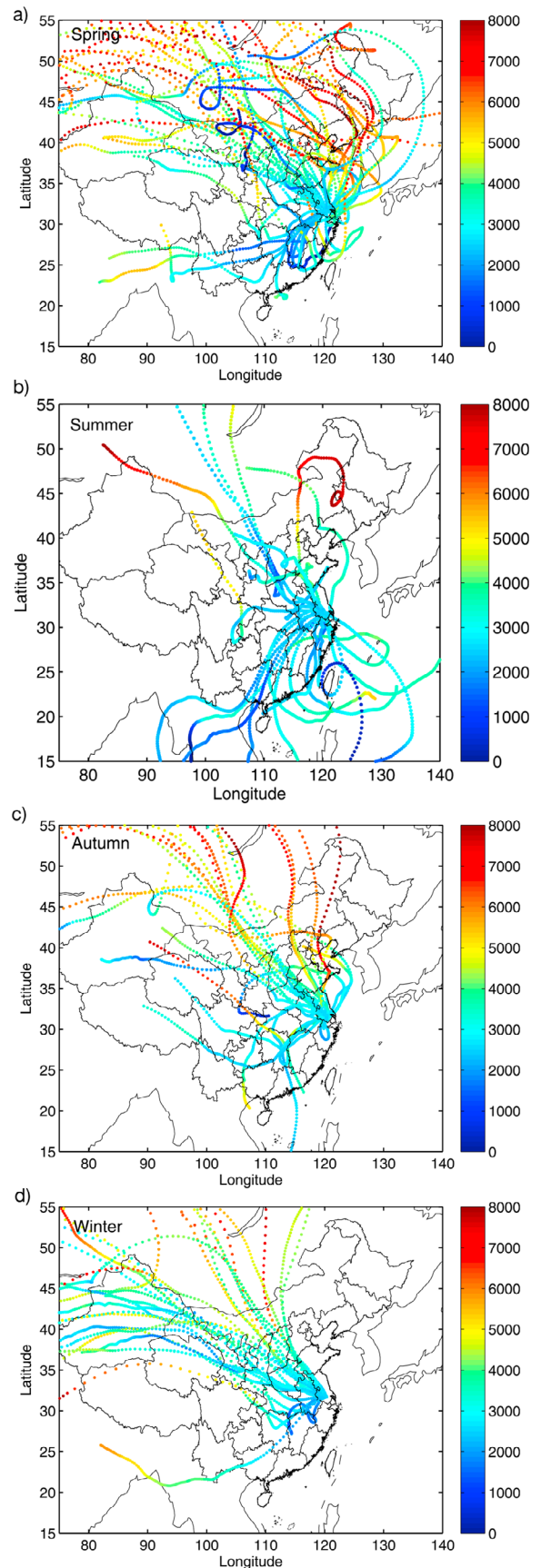
Figure 10. Same as Figure 9 but ending at 2.5-km AGL.

Table 2. Eight Groups of Back Trajectories Identified and Their Source Regions and Paths Taken Before Reaching Taihu

Group	Source Region	Path Taken Before Reaching Taihu
1	Mongolia, Siberia or northern China	Over the heavily polluted interior and coastal areas of northern China
2	Mongolia, Siberia or northern China	Over the interior of northern China, then over the East China Sea
3	Clean marine atmosphere	Densely populated eastern/southeastern regions of China
4	Northwestern China	Across the Hexi region and the Loess Plateau
5	Southeastern inland region	Southeastern coast of China
6	Southwestern part of China	Southwest of the site
7	Indochina	Northward over southeastern China
8	Local	Local

[27] In winter when strong westerlies prevail [*Kim et al.*, 2007], the bulk of the back trajectories arriving at both 0.5-km and 2.5-km levels over Taihu trace to the remote interior of Mongolia and Siberia and northwestern China (Figures 9d and 10d). At the 0.5-km level, they travel over the coastal areas of north China (Group 1) and through the "dust corridor" (Group 4) with only 7.7% of these cases passing over the East China Sea before arriving at the site (Group 2). At the 2.5-km level, the majority of the cases also find their way to Taihu via the interior of northern China (Group 1).

3.3. Role of Dust Aerosols on Aerosol Vertical Distribution

[28] By virtue of the polarization sensitivity of the MPL deployed at Taihu, the role of non-spherical particles, and in particular, dust, on the seasonal vertical distribution of aerosols is investigated. Polarized lidar measurements can be used to determine the characteristic parameter "d" of the Mueller matrix describing the polarizing effects from randomly oriented particles in the atmosphere [*Flynn et al.*, 2007]. Specifically, the parameter "d" identifies the degree to which the scattering event modifies the polarization vector. In the absence of multiple scattering, "d" is near zero for spherical particles and greater than zero for non-spherical particles. The parameter "d" is explicitly related to the commonly described lidar "linear depolarization ratio" δ_{linear}, a potential tool for differentiating different aerosol types [*Sakai et al.*, 2000; *Rajeev et al.*, 2010].

[29] The following criteria are used to identify dust with a high probability of mixing with local emissions: (1) δ_{linear} must be larger than 0.1 [*Cavalieri et al.*, 2010] in at least five consecutive vertical bins for most of the day; (2) at least one of the five-day back trajectories arriving at the 0.5-km and 2.5-km levels over Taihu pointed to the dust source region or passes over it before reaching the site; (3) no precipitation is detected during the time it takes for the air mass to arrive at the site; and (4) dust activities are detected near the site on the day in question or in the dust region before the air mass arrives at the site, based upon the aerosol index from NASA's Ozone Monitoring Instrument (OMI) and surface observations from the dust monitoring network established by the China Meteorological Administration (http://www.duststorm.com.cn/).

[30] The linear depolarization value of 0.1 we apply indicates the presence of dust (which is generally mixed with other spherical particles, known as polluted dust, over Taihu). This is lower than dust particle linear depolarization from several studies at other locations, such as ~0.3 over North Africa [*Z. Liu et al.*, 2011], 0.31 for pure Saharan mineral dust [*Freudenthaler et al.*, 2009], and ~0.2 over Chungli, Taiwan, during a strong Asian dust storm event [*Nee et al.*, 2007]. However, most of these studies focused on pure dust particles near source regions or strong dust activities located away from dust regions, where the non-spherical dust particle fraction is much larger than the spherical particle fraction. This value chosen for δ_{linear} (0.1) is similar to the threshold value used for identifying polluted dust in the Cloud-Aerosol Lidar and Infrared Pathfinder Satellite Observation (CALIPSO) automated aerosol classification algorithm [*Omar et al.*, 2009] and for defining weak/moderate dust layers by *Mishra et al.* [2010]. Using these criteria, 13, 6, and 7 vertical extinction profiles in spring, autumn, and winter, respectively, were identified as under the influence of dust aerosols. None of the summertime profiles indicated any dust activity.

[31] Figure 11 presents rich quantitative information about the vertical profiles of aerosols obtained from polarized lidar measurements. These images illustrate the intensity of the normalized relative backscatter (NRB) (Figures 11a and 11c) and the $\log_{10}$ of linear depolarization ratio (Figures 11b and 11d). Figures 11a and 11b and Figures 11c and 11d show images of lidar profiles for relatively dust-free conditions (January 2, 2009) and heavy dust conditions (March 16, 2009), respectively, with the strikingly different linear depolarization ratios indicative of the very different aerosol types on these two days. It is apparent that Figures 11a and 11b correspond a day with a well-defined boundary layer dominated by spherical particles and a slightly elevated aerosol layer while Figures 11c and 11d show an abundance of highly depolarizing aerosols at the surface for much of the day along with extensive elevated layers exhibiting varying depolarizing properties.

[32] Figure 12 shows seasonal mean aerosol extinction profiles in the presence of dust (red lines) and absence of dust (black lines) in spring, autumn and winter; horizontal bars represent standard deviations. Differences in extinction between dusty and non-dusty cases in spring and fall are greater than during wintertime. In spring, from the surface to 2.5 km and between 3 km and 4.5 km, aerosol extinction coefficients in the presence of dust are larger than those in the absence of dust, illustrating that dust aerosols enhance aerosol extinction near the surface and at higher altitudes [*Tsai et al.*, 2008; *Rajeev et al.*, 2010; *J. Liu et al.*, 2011]. Between 0.5 km and 1.5 km in autumn, aerosol extinction coefficients in the presence of dust are smaller than those in its absence, indicating that non-dust aerosol particles contribute to larger values of extinction. No significant
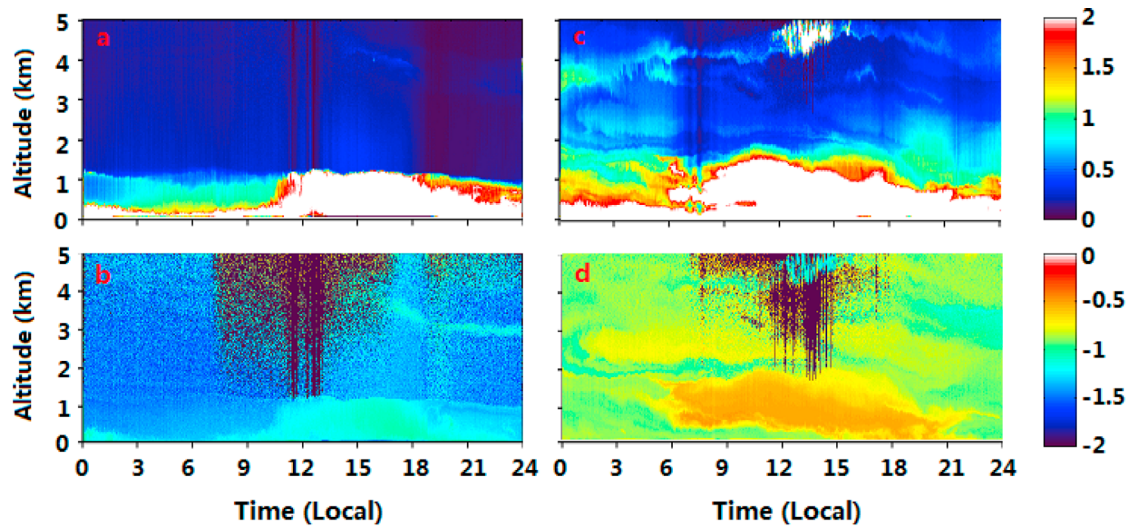
Figure 11. (a and c) The intensity of the normalized relative backscatter (NRB) and the (b and d) logarithm of linear depolarization ratio on a dust-free day (Figures 11a and 11b: January 2, 2009) and a dusty day (Figures 11c and 11d: March 16, 2009).

difference between wintertime extinction profiles is found for dusty and non-dusty cases. No significant elevated dust layers were detected, which may be due to dust transport patterns and dust deposition in the lower atmosphere, which is typical in eastern and southern China [*Zhou et al.*, 2002; *Tsai et al.*, 2008].

3.4. Aerosol Radiative Effects

[33] The Santa Barbara DISORT Atmospheric Radiative Transfer (SBDART) model [*Ricchiazzi et al.*, 1998] is used

to estimate broadband (0.25 to 4.0 μm) total, diffuse, and direct shortwave irradiances and to evaluate aerosol particle direct radiative effects. It is based on the low-resolution band models developed for LOWTRAN 7 atmospheric transmission and the DISORT radiative transfer model. Inputs to the model include the vertical profiles of water vapor and ozone, obtained by partitioning total column water vapor amounts from AERONET retrievals and ozone amounts from OMI according to a standard model atmosphere [*McClatchey et al.*, 1972]. Aerosol particle extinction coefficient profiles
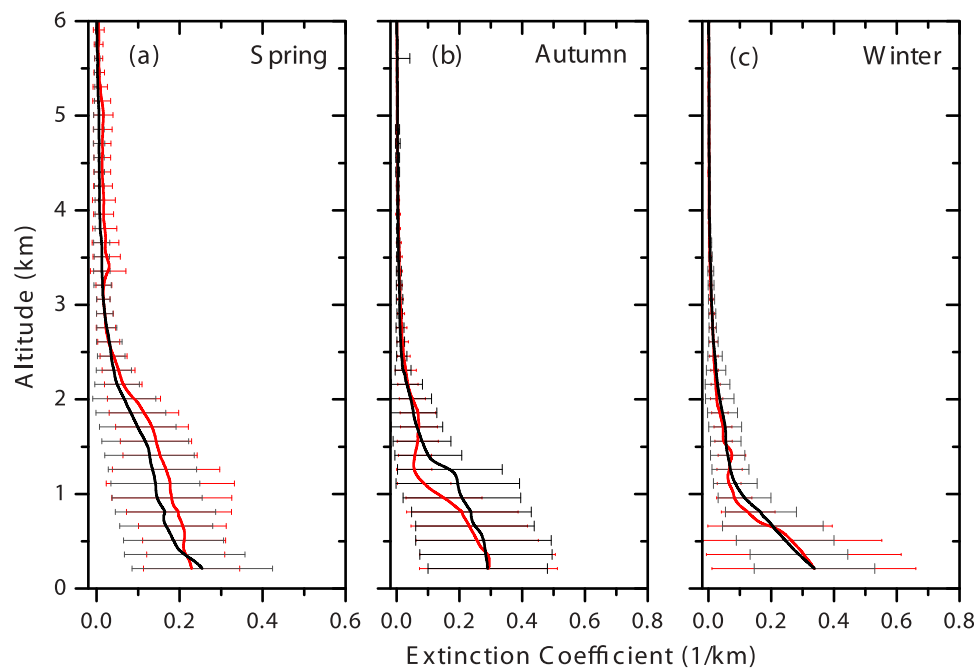

Figure 12. Seasonal mean aerosol extinction coefficient profiles at 527 nm for cases with dust (red lines) and without (black lines) in (a) spring, (b) autumn and (c) winter from June 2008 to May 2009. Horizontal bars represent standard deviations.
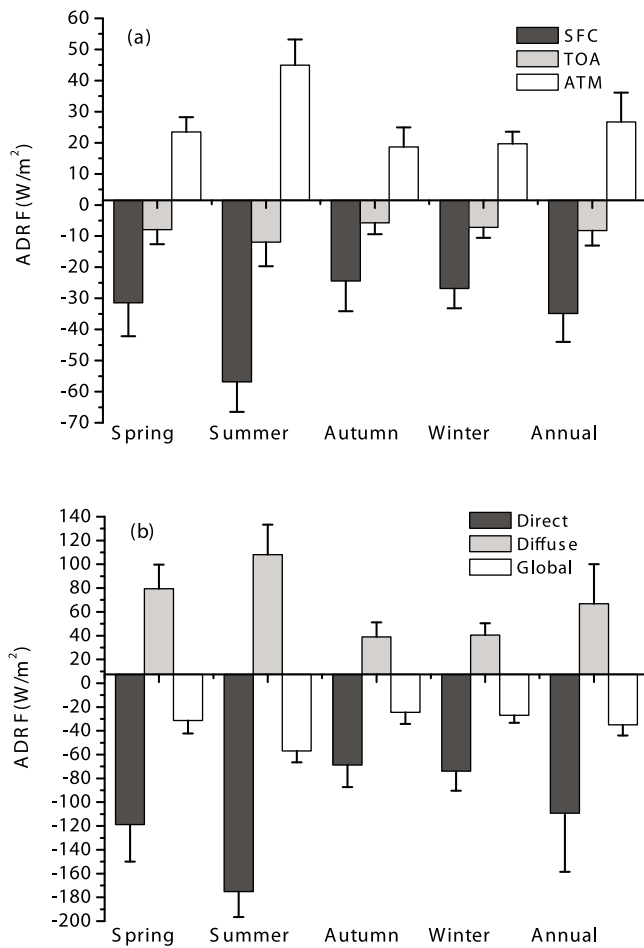
Figure 13. (a) Seasonal and annual aerosol direct radiative forcing (ADRF) at the surface (SFC), the top-of-the-atmosphere (TOA), and within the atmosphere (ATM) and (b) seasonal changes in surface downwelling global, direct and diffuse shortwave irradiances induced by aerosols over the period of June 2008 to May 2009.

were derived from the MPL, normalized by total AOD from the Cimel, while SSA and ASY were assumed constant as derived following AERONET. The aerosol properties, including AOD, SSA and ASY at four AERONET wavelengths (i.e., 440 nm, 675 nm, 870 nm, and 1020 nm) were used to interpolate and extrapolate into the spectral divisions of the SBDART model [Xia et al., 2007]. Surface albedo data were applied from the MODIS Level 2 Collection 5 spectral surface reflectance product (MOD09). Shortwave irradiances under cloud-free conditions were simulated with and without aerosol particles and were then used to determine aerosol direct radiative forcing (ADRF) at the surface (SFC) and at the TOA. A previous study shows that SBDART simulations of downwelling broadband flux at the surface agrees exceptionally well with ground-based measurements, and that modeled upwelling TOA fluxes were compatible with Clouds and Earth's Radiant Energy System satellite retrievals in terms of absolute differences [Li et al., 2010]. They also showed that the combined error caused by uncertainties in main input parameters, including AOD,

α, SSA, ASY, surface reflectance, and ozone amounts, is 8.76 ± 3.44 W/m^2.

[34] ADRF is commonly used term for quantifying the direct effect of aerosols on the atmospheric energy budget. It is usually expressed as instantaneous or diurnal mean radiative forcing [Xia et al., 2007]. The definition of diurnal mean radiative forcing is often given as

$$dF = \frac{1}{24h} \int F(t)dt,$$

where $F(t)$ represents instantaneous radiative forcing values. The aerosol radiative forcing within the atmosphere (ATM) is defined as the difference between radiative forcings at the TOA and SFC.

[35] The left plot in Figure 13a depicts the seasonal and annual mean diurnally averaged ADRF during the study period. Note that ADRF in summer is for June only because there were no SSA and ASY retrievals made in July and August. Annual mean ADRF estimates at the SFC, the TOA and within the ATM were -34.8 ± 9.1, -8.2 ± 4.8 and 26.7 ± 9.4 W/m^2, respectively. The magnitude of ADRF at the SFC is comparable with values reported in other studies made in eastern China for different periods (usually one year) or different locations. For example, the largest negative values for ADRF at the surface ranged from -32 to -20 W/m^2 over eastern China [Li et al., 2010]. Xia et al. [2007] reported that the annual mean SFC ADRF at Taihu was -38.4 W/m^2, based on ground-based radiation measurements collected from September 2005 to August 2006. Global mean estimates of ADRF at the SFC, at the TOA, and within the ATM from observations over land are -11.9, -4.9 and 7.0 W/m^2, respectively, and from modeling, are -7.6, -3.0 and 4.0 W/m^2, respectively [H. Yu et al., 2006, 2009]. The magnitudes of ADRF at the SFC and within the ATM at Taihu are more than three times greater than global mean values over land [Yu et al., 2006; Xia et al., 2007], implying strong cooling at the surface and warming of the lower troposphere. Relatively high RH over eastern China can partly explain the large aerosol cooling effect at the SFC because the ADRF estimate within the surface boundary layer is strongly dependent on RH [Cheng et al., 2008]. Enhanced warming within the lower troposphere is not surprising because eastern China experiences high aerosol mass loading and an abundance of absorbing aerosol particles like smoke [Li et al., 2007].

[36] It is important to understand how relative proportions of direct and diffuse downwelling surface fluxes are modulated by the presence of aerosols. For example, Gu et al. [2002] found that diffuse radiation results in higher light use efficiencies by plant canopies, which has implications for the study of the global carbon cycle. Figure 13b shows seasonal and annual diurnal mean values of ADRF for global, direct and diffuse radiation. In the presence of aerosols, direct shortwave fluxes reaching the surface were reduced by -109.2 ± 49.4 W/m^2 and diffuse shortwave fluxes were enhanced by 66.8 ± 33.3 W/m^2 in terms of annual means.

[37] The aerosol radiative forcing efficiency (ARFE) is the rate at which irradiance within a certain wavelength range changes per unit of AOD, and is an indicator of the radiative forcing potential of a given type of composite aerosol
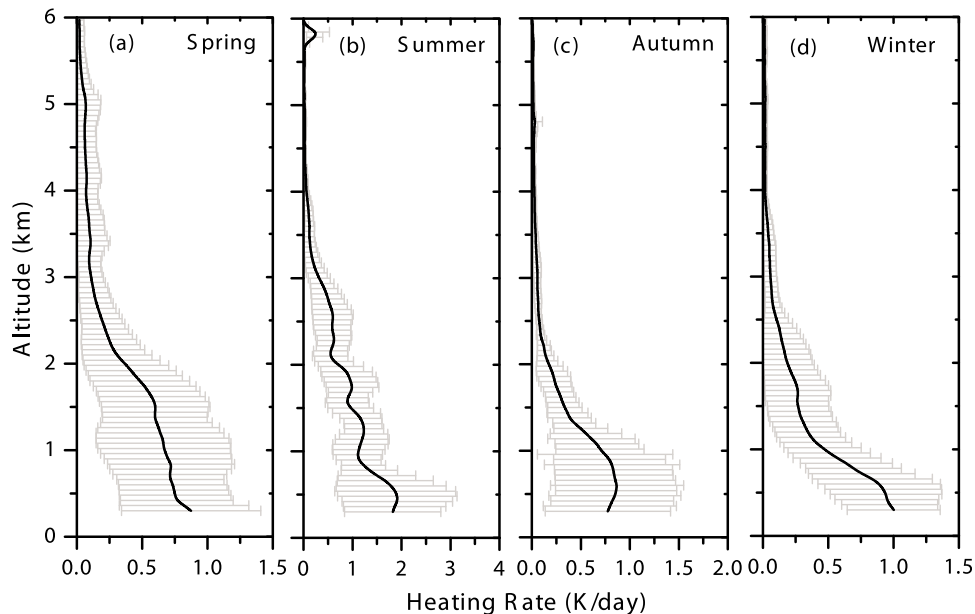
Figure 14. Seasonal mean aerosol heating rate profiles over Taihu in (a) spring, (b) summer, (c) autumn, and (d) winter from June 2008 to May 2009. Horizontal lines represent standard deviations.

[*Pathak et al.*, 2010]. It is also useful for quantifying and comparing aerosol particle radiative effects, as well as seeing more clearly how their optical properties impact ADRF at different sites under a wide range of conditions [*Yu et al.*, 2006; *Wang et al.*, 2010]. The annual mean magnitudes of ARFE in our study were -54.4 ± 5.3, -13.1 ± 1.5 and 41.3 ± 4.6 Wm^{-2} τ^{-1} at the SFC, TOA and ATM, respectively, which are significantly larger than the mean values over China given by *Li et al.* [2010] (-35.1, -0.5 and 34.1 Wm$^{-2}\tau^{-1}$ at the SFC, TOA and ATM, respectively). However, the ARFE at the SFC at Taihu is clearly smaller than that calculated at some cities in northern China, such as Xianghe (-65.4 ± 4.7 Wm^{-2} τ^{-1}) and Beijing (-61.2 ± 3.5 Wm^{-2} τ^{-1}) [*Li et al.*, 2010]. For context, studies made at other locations show that mean ARFE at the SFC at the Kaashidhoo Climate Observatory (KCO), Maldives is -72.2 ± 5.5 Wm^{-2} τ^{-1} [*Bush and Valero*, 2002], -75 Wm^{-2} τ^{-1} over the Indian Ocean [*Ramanathan et al.*, 2001a], -85 Wm^{-2} τ^{-1} in the Middle East [*Markowicz et al.*, 2002], -83 Wm^{-2} τ^{-1} over northeastern India [*Pathak et al.*, 2010], and -89.4 Wm^{-2} τ^{-1} induced by black carbon and organic carbon aerosol over the South Asian region [*Wang et al.*, 2007].

[38] No previous studies conducted in China attempt to apportion the radiative energy trapped in the atmosphere in the presence of aerosols from the surface to the upper atmosphere. Thanks to lidar measurements available for this study, this term is computed here in terms of the radiative heating rate, which is an indicator of the climatic impact of aerosols, and defined as

$$\frac{dT}{dt} = -\frac{g}{C_p}\frac{dF}{dP},$$

where $\frac{dT}{dt}$ is the heating rate (K/day), g is the acceleration due to gravity, C_p is the specific heat capacity of dry air at constant pressure, F is the atmospheric forcing and dP is the change in atmospheric pressure. 527 nm particle extinction profiles retrieved from the MPL provide key information describing vertical particle distributions, which is the first of many factors influencing the radiative heating rate. Unfortunately, vertical profiles of SSA require multiwavelength approaches [*Cattrall et al.*, 2005]. As such, the column-mean SSA derived by AERONET is assumed in this investigation.

[39] Figure 14 shows seasonal diurnal mean vertical profiles of aerosol particle heating rate (black solid lines), with corresponding standard deviations (gray horizontal lines). The vertical distribution of heating rate is consistent with the vertical distribution of mean aerosol extinction coefficients (i.e., as the aerosol particle extinction coefficient increases, the heating rate increases). The maximum heating rate was 0.87, 1.91, 0.87 and 1.00 K/day in spring, summer (June only), autumn and winter, respectively. The heating rate in summer does not vary smoothly with height, which implies that the energy distribution at different altitudes can significantly change. This would modify atmospheric static stability and influence convection [*Ramanathan et al.*, 2001b]. In spring, the heating rate is fairly constant within the mixed layer of the atmosphere. In autumn, the heating rate increases with height. This would have an impact on convective instability and thermal profiles, which could induce inversions at lower altitudes, which is not conducive to lofting of pollutants from near the surface. The relatively large change in heating rate with height within the lower troposphere in winter would also have a significant impact on convective instability. From the surface to 2 km, the annual mean heating rate due to aerosols is 0.74 K/day with seasonal means of 0.64, 1.26, 0.56 and 0.50 K/day in spring, summer, autumn and winter, respectively.

[40] One uncertainty in the calculated ADRF and heating rate profiles is the lack of knowledge about the vertical variability of aerosol optical properties, especially SSA. *Guan et al.* [2010] found that the difference in radiative

forcing for different SSA profiles is small at the surface, while at the TOA a change of ~10% occurs if absorbing aerosol is assumed in the elevated layer in lieu of all absorption occurring in the boundary layer. These uncertainties become obvious when radiative transfer calculations assume a constant column-mean SSA for the multilayer aerosol vertical distribution, especially when aerosols originate from different source regions for each layer [*Wang et al.*, 2010]. Based on lidar depolarization measurements, elevated dust layers were not found, although, this does not rule out changes in particle properties such as size or composition. No cases of multiple aerosol layers were found that decrease associated uncertainties in our calculations. *McFarlane et al.* [2009] provide some suggestions on improving our understanding of the vertical distribution of aerosol optical properties, such as use of a multiple wavelength lidar or a combination of the MFRSR with longwave sensors.

4. Conclusions

[41] Four years of aerosol particle optical properties (2006–2009) and a one-year vertical profiles of aerosol extinction coefficient (June 2008 to May 2009) were measured by ground-based sun/sky radiometer and a polarization-sensitive micropulse lidar at Taihu, an observation site in eastern China. Seasonal patterns in aerosol optical properties and vertical structure, as well as the influence of aerosols on solar radiation and solar heating, are described.

[42] Multiyear (2006–2009) means of AOD at 500 nm, α at 440–675 nm, SSA and ASY at 675 nm are 0.74 ± 0.45, 1.20 ± 0.27, 0.912 ± 0.035 and 0.655 ± 0.036, respectively, with moderate inter-annual variations. The occurrence of high AOD indicates that relatively heavy aerosol loading prevails year-round at the site. Seasonal mean AOD (α) during the four-year period shows a maximum in summer (autumn) and minimum in winter (spring). Relatively larger (smaller) values of SSA and ASY occurred in summer (winter). The wide variability of aerosol optical properties illustrates the complexity of aerosol particle type and optical characteristics found at this location.

[43] The vertical distribution of aerosol particles found each season is relatively consistent. A maximum in the aerosol particle extinction coefficient at 527 nm is found near the surface and gradually decreases with height. The majority of aerosol particles were located below 2 km, and about 62%, 67%, 67% and 83% of total particle loadings were below 1 km in spring, summer, autumn and winter, respectively. A relatively large fraction of solar radiation can be absorbed within the lower troposphere due to the presence of high aerosol loading there. Strong near-surface aerosol particle extinction coefficients were associated with relatively strong easterly, southeasterly and westerly winds (wind speeds greater than 4 m/s), suggesting that the regional transport of locally generated aerosol particles from densely populated areas surrounding the site may contribute to loading at the surface at Taihu. By means of 5-day back trajectory analyses, the majority of air masses ending at 0.5-km and 2.5-km AGL at the Taihu were tracked to northern/northwestern China, as well as remote regions of Mongolia and Siberia, in spring, autumn and winter. In summer, air masses originate over the seas to the east of the

site. A relatively larger influence of dust on particle vertical distributions in spring and autumn was found, while much smaller effects appeared in winter. Dust aerosols not only enhanced particle extinction coefficients at high altitudes, but also at low altitudes in spring.

[44] Heavy aerosol loading at Taihu results in significant warming of the lower troposphere and cooling at the surface. Annual mean ADRF estimated at the SFC, at the TOA and within the ATM were -34.8 ± 9.1, -8.2 ± 4.8 and 26.7 ± 9.4 W/m^2, respectively. Corresponding annual mean aerosol direct shortwave radiative efficiencies were -54.4 ± 5.3, -13.1 ± 1.5 and 41.3 ± 4.6 Wm^{-2} τ^{-1} at the SFC, at the TOA and within the ATM, respectively. Aerosols dramatically impact global irradiance, but also significantly change the fraction of direct and diffuse components of surface global irradiance reaching the surface. The annual mean decrease in direct and increase in diffuse downwelling shortwave radiation at the surface are -109.2 ± 49.4, and 66.8 ± 33.3 W/m^2, respectively.

[45] The relatively high magnitude of solar radiation absorbed by the atmosphere in the presence of aerosol particles is a significant source of heating to the atmosphere, especially within the lower troposphere. This can change the vertical distribution of the atmospheric heating rate, thus change the atmospheric temperature structure, as well as influence regional atmospheric static stability, dynamic system and pollution events, regional circulation and climate. From the surface to 2 km, the annual mean heating rate due to aerosol particles over Taihu is 0.74 K/day, with seasonal means of 0.64, 1.26, 0.56 and 0.50 K/day in spring, summer, autumn and winter, respectively.

[46] The results showed the allocation of the radiative energy trapped in the atmosphere in the presence of aerosols from the surface to the upper atmosphere over this high aerosol-loading area in China, which is very important to evaluate the aerosol climate effects. It helps improve our understanding of the seasonal variations in aerosol optical properties and decrease uncertainties in the estimation of aerosol direct effects both at the surface and in the atmospheric column. More importantly, the vertical profiles of heating induced by aerosols are the key to understand their impact on atmospheric dynamics, especially feedbacks between pollution and boundary layer development, which will be addressed in our future studies.

References

Ackerman, A. S., O. B. Toon, D. E. Stevens, A. J. Heymsfield, V. Ramanathan, and E. J. Welton (2000), Reduction of tropical cloudiness by soot, *Science*, *288*, 1042–1047, doi:10.1126/science.288.5468.1042.

Alexandrov, M. D., A. Marshak, B. Cairns, A. A. Lacis, and B. E. Carlson (2004), Automated cloud screening algorithm for MFRSR data, *Geophys. Res. Lett.*, *31*, L04118, doi:10.1029/2003GL019105.

Alexandrov, M. D., A. A. Lacis, B. E. Carlson, and B. Cairns (2008), Characterization of atmospheric aerosols using MFRSR measurements, *J. Geophys. Res.*, *113*, D08204, doi:10.1029/2007JD009388.

Bush, B. C., and F. P. J. Valero (2002), Spectral aerosol radiative forcing at the surface during the Indian Ocean Experiment (INDOEX), *J. Geophys. Res.*, *107*(D19), 8003, doi:10.1029/2000JD000020.

Campbell, J. R., D. L. Hlavka, E. J. Welton, C. J. Flynn, D. D. Turner, J. D. Spinhirne, V. S. Scott, and I. H. Hwang (2002), Full-time, eye-safe cloud and aerosol lidar observation at Atmospheric Radiation Measurement Program sites: Instrument and data processing, *J. Atmos. Oceanic Technol.*, *19*, 431–442, doi:10.1175/1520-0426(2002)019<0431:FTESCA>2.0.CO;2.

Campbell, J. R., K. Sassen, and E. J. Welton (2008), Elevated cloud and aerosol layer retrievals from micropulse lidar signal profiles, *J. Atmos. Oceanic Technol.*, *25*, 685–700, doi:10.1175/2007JTECHA1034.1.

Cattrall, C., J. Reagan, K. Thome, and O. Dubovik (2005), Variability of aerosol and spectral lidar and backscatter and extinction ratios of key aerosol types derived from selected Aerosol Robotic Network locations, *J. Geophys. Res.*, *110*, D10S11, doi:10.1029/2004JD005124.

Cavalieri, O., et al. (2010), Variability of aerosol vertical distribution in the Sahel, *Atmos. Chem. Phys. Discuss.*, *10*(7), 17,609–17,655, doi:10.5194/acpd-10-17609-2010.

Cheng, Y. F., et al. (2008), Relative humidity dependence of aerosol optical properties and direct radiative forcing in the surface boundary layer at Xinken in Pearl River Delta of China: An observation based numerical study, *Atmos. Environ.*, *42*(25), 6373–6397, doi:10.1016/j.atmosenv.2008.04.009.

Chew, B. N., J. R. Campbell, J. S. Reid, D. M. Giles, E. J. Welton, S. V. Salinas, and S. C. Liew (2011), Tropical cirrus cloud contamination in Sun photometer data, *Atmos. Environ.*, *45*(37), 6724–6731, doi:10.1016/j.atmosenv.2011.08.017.

Chou, M. D., P. H. Lin, P. L. Ma, and H. J. Lin (2006), Effects of aerosols on the surface solar radiation in a tropical urban area, *J. Geophys. Res.*, *111*, D15207, doi:10.1029/2005JD006910.

Clarke, A., and V. Kapustin (2010), Hemispheric aerosol vertical profiles: Anthropogenic impacts on optical depth and cloud nuclei, *Science*, *329*, 1488–1492, doi:10.1126/science.1188838.

Dubovik, O., A. Smirnov, B. N. Holben, M. D. King, Y. J. Kaufman, T. F. Eck, and I. Slutsker (2000), Accuracy assessments of aerosol optical properties retrieved from AERONET Sun and sky radiance measurements, *J. Geophys. Res.*, *105*, 9791–9806, doi:10.1029/2000JD900040.

Engling, G., and A. Gelencser (2010), Atmospheric brown clouds: From local air pollution to climate change, *Elements*, *6*, 223–228, doi:10.2113/gselements.6.4.223.

Fernald, F. G. (1984), Analysis of atmospheric lidar observations: Some comments, *Appl. Opt.*, *23*, 652–653, doi:10.1364/AO.23.000652.

Flynn, C. J., A. Mendoza, Y. Zheng, and S. Mathur (2007), Novel polarization-sensitive micropulse lidar measurement technique, *Opt. Express*, *15*(6), 2785–2790, doi:10.1364/OE.15.002785.

Forster, P. et al. (2007), Changes in atmospheric constituents and in radiative forcing, in *Climate Change 2007: The Physical Science Basis. Contribution of Working Group I to the Fourth Assessment Report of the Intergovernmental Panel on Climate Change*, edited by S. Solomon et al., pp. 129–234, Cambridge Univ. Press, Cambridge, U. K.

Freudenthaler, V., et al. (2009), Depolarization ratio profiling at several wavelengths in pure Saharan dust during SAMUM 2006, *Tellus, Ser. B*, *61*(1), 165–179, doi:10.1111/j.1600-0889.2008.00396.x.

Gu, L., D. Baldocchi, S. B. Verma, T. A. Black, T. Vesala, E. M. Falge, and P. R. Dowty (2002), Advantages of diffuse radiation for terrestrial ecosystem productivity, *J. Geophys. Res.*, *107*(D6), 4050, doi:10.1029/2001JD001242.

Guan, H., B. Schmid, A. Bucholtz, and R. Bergstrom (2010), Sensitivity of shortwave radiative flux density, forcing, and heating rate to the aerosol vertical profile, *J. Geophys. Res.*, *115*, D06209, doi:10.1029/2009JD012907.

Harrison, L., and J. Michalsky (1994), Objective algorithms for the retrieval of optical depths from ground-based measurements, *Appl. Opt.*, *33*, 5126–5132, doi:10.1364/AO.33.005126.

He, Q., C. Li, J. T. Mao, A. K. H. Lau, and D. A. Chu (2008), Analysis of aerosol vertical distribution and variability in Hong Kong, *J. Geophys. Res.*, *113*, D14211, doi:10.1029/2008JD009778.

Holben, B. N., et al. (1998), AERONET—A federated instrument network and data archive for aerosol characterization, *Remote Sens. Environ.*, *66*, 1–16, doi:10.1016/S0034-4257(98)00031-5.

Huang, J., N. C. Hsu, S.-C. Tsay, M.-J. Jeong, B. N. Holben, T. A. Berkoff, and E. J. Welton (2011), Susceptibility of aerosol optical thickness retrievals to thin cirrus contamination during the BASE-ASIA campaign, *J. Geophys. Res.*, *116*, D08214, doi:10.1029/2010JD014910.

Huebert, B. J., T. Bates, P. B. Russell, G. Shi, Y. J. Kim, K. Kawamura, G. Carmichael, and T. Nakajima (2003), An overview of ACE-Asia: Strategies for quantifying the relationships between Asian aerosols and their climatic impacts, *J. Geophys. Res.*, *108*(D23), 8633, doi:10.1029/2003JD003550.

Jeong, M. J., Z. Li, E. Andrews, and S.-C. Tsay (2007), Effect of aerosol humidification on the column aerosol optical thickness over

the Atmospheric Radiation Measurement Southern Great Plains site, *J. Geophys. Res.*, *112*, D10202, doi:10.1029/2006JD007176.

Johnson, B. T., B. Heese, S. A. McFarlane, P. Chazette, A. Jones, and N. Bellouin (2008), Vertical distribution and radiative effects of mineral dust and biomass burning aerosol over West Africa during DABEX, *J. Geophys. Res.*, *113*, D00C12, doi:10.1029/2008JD009848.

Kalnay, E., et al. (1996), The NCEP/NCAR 40-year reanalysis project, *Bull. Am. Meteorol. Soc.*, *77*, 437–471, doi:10.1175/1520-0477(1996)077<0437:TNYRP>2.0.CO;2.

Kaufman, Y. J., I. Koren, L. A. Remer, D. Rosenfeld, and Y. Rudich (2005), The effect of smoke, dust, and pollution aerosol on shallow cloud development over the Atlantic Ocean, *Proc. Natl. Acad. Sci. U. S. A.*, *102*, 11,207–11,212, doi:10.1073/pnas.0505191102.

Kim, S. W., S. C. Yoon, J. Y. Kim, and S. Y. Kim (2007), Seasonal and monthly variations of columnar aerosol optical properties over East Asia determined from multi-year MODIS, LIDAR, and AERONET Sun/sky radiometer measurements, *Atmos. Environ.*, *41*(8), 1634–1651, doi:10.1016/j.atmosenv.2006.10.044.

Lau, K.-M., et al. (2008), The joint aerosol monsoon experiment, A new challenge for monsoon climate research, *Bull. Am. Meteorol. Soc.*, *89*, 369–383, doi:10.1175/BAMS-89-3-369.

Lee, K. H., Z. Li, M. C. Cribb, J. Liu, L. Wang, Y. Zheng, X. Xia, H. Chen, and B. Li (2010), Aerosol optical depth measurements in eastern China and a new calibration method, *J. Geophys. Res.*, *115*, D00K11, doi:10.1029/2009JD012812.

Léon, J. F., Y. Derimian, I. Chiapello, D. Tanré, T. Podvin, B. Chatenet, A. Diallo, and C. Deroo (2009), Aerosol vertical distribution and optical properties over M'Bour (16.96°W; 14.39°N), Senegal from 2006 to 2008, *Atmos. Chem. Phys.*, *9*(23), 9249–9261, doi:10.5194/acp-9-9249-2009.

Li, Z., et al. (2007), Preface to special section on East Asian Studies of Tropospheric Aerosols: An International Regional Experiment (EAST-AIRE), *J. Geophys. Res.*, *112*, D22S00, doi:10.1029/2007JD008853.

Li, Z., K. H. Lee, Y. Wang, J. Xin, and W. M. Hao (2010), First observation-based estimates of cloud-free aerosol radiative forcing across China, *J. Geophys. Res.*, *115*, D00K18, doi:10.1029/2009JD013306.

Li, Z., F. Niu, J. Fan, Y. Liu, D. Rosenfeld, and Y. Ding (2011a), Long-term impacts of aerosols on the vertical development of clouds and precipitation, *Nat. Geosci.*, *4*, 888–894, doi:10.1038/ngeo1313.

Li, Z., et al. (2011b), East Asian Studies of Tropospheric Aerosols and their Impact on Regional Climate (EAST-AIRC): An overview, *J. Geophys. Res.*, *116*, D00K34, doi:10.1029/2010JD015257.

Liu, D., Z. Wang, Z. Y. Liu, D. Winker, and C. Trepte (2008), A height resolved global view of dust aerosols from the first year CALIPSO lidar measurements, *J. Geophys. Res.*, *113*, D16214, doi:10.1029/2007JD009776.

Liu, J., Y. Zheng, Z. Li, C. Flynn, E. J. Welton, and M. Cribb (2011), Transport, vertical structure and radiative properties of dust events in southeast China determined from ground and space sensors, *Atmos. Environ.*, *45*(35), 6469–6480, doi:10.1016/j.atmosenv.2011.04.031.

Liu, Z., D. Winker, A. Omar, M. Vaughan, C. Trepte, Y. Hu, K. Powell, W. Sun, and B. Lin (2011), Effective lidar ratios of dense dust layers over North Africa derived from the CALIOP measurements, *J. Quant. Spectrosc. Radiat. Transfer*, *112*(2), 204–213, doi:10.1016/j.jqsrt.2010.05.006.

Markowicz, K. M., P. J. Flatau, M. V. Ramana, P. J. Crutzen, and V. Ramanathan (2002), Absorbing Mediterranean aerosols lead to a large reduction in the solar radiation at the surface, *Geophys. Res. Lett.*, *29*(20), 1968, doi:10.1029/2002GL015767.

McClatchey, R. A., R. W. Fenn, J. E. A. Selby, F. E. Volz, and J. S. Garing (1972), Optical properties of the atmosphere, 3rd ed., *Environ. Res. Pap. 411*, 113 pp., AFCRL, Hanscom AFB, Mass.

McFarlane, S. A., E. I. Kassianov, J. Barnard, C. Flynn, and T. P. Ackerman (2009), Surface shortwave aerosol radiative forcing during the Atmospheric Radiation Measurement mobile facility deployment in Niamey, Niger, *J. Geophys. Res.*, *114*, D00E06, doi:10.1029/2008JD010491.

McFarquhar, G. M., and H. L. Wang (2006), Effects of aerosols on trade wind cumuli over the Indian Ocean: Model simulations, *Q. J. R. Meteorol. Soc.*, *132*, 821–843, doi:10.1256/qj.04.179.

Mishra, M. K., K. Rajeev, B. V. Thampi, K. Parameswaran, and A. K. M. Nair (2010), Micro pulse lidar observations of mineral dust layer in the lower troposphere over the southwest coast of Peninsular India during the Asian summer monsoon season, *J. Atmos. Sol. Terr. Phys.*, *72*(17), 1251–1259, doi:10.1016/j.jastp.2010.08.012.

Nakajima, T., et al. (2003), Significance of direct and indirect radiative forcings of aerosols in the East China Sea region, *J. Geophys. Res.*, *108*(D23), 8658, doi:10.1029/2002JD003261.

Nakajima, T., et al. (2007), Overview of the Atmospheric Brown Cloud East Asian Regional Experiment 2005 and a study of the aerosol direct

radiative forcing in East Asia, *J. Geophys. Res.*, *112*, D24S91, doi:10.1029/2007JD009009.

Nee, J. B., C.-W. Chiang, H.-L. Hu, S.-X. Hu, and J.-Y. Yu (2007), Lidar measurements of Asian dust storms and dust cloud interactions, *J. Geophys. Res.*, *112*, D15202, doi:10.1029/2007JD008476.

Niu, F., Z. Li, C. Li, K.-H. Lee, and M. Wang (2010), Increase of wintertime fog in China: Potential impacts of weakening of the Eastern Asian monsoon circulation and increasing aerosol loading, *J. Geophys. Res.*, *115*, D00K20, doi:10.1029/2009JD013484.

Omar, A. H., et al. (2009), The CALIPSO automated aerosol classification and lidar ratio selection algorithm, *J. Atmos. Oceanic Technol.*, *26*(10), 1994–2014, doi:10.1175/2009JTECHA1231.1.

Pan, L., H. Che, F. H. Geng, X. A. Xia, Y. Q. Wang, C. Z. Zhu, M. Chen, W. Gao, and J. P. Guo (2010), Aerosol optical properties based on ground measurements over the Chinese Yangtze Delta region, *Atmos. Environ.*, *44*(21–22), 2587–2596, doi:10.1016/j.atmosenv.2010.04.013.

Pathak, B., G. Kalita, K. Bhuyan, P. K. Bhuyan, and K. K. Moorthy (2010), Aerosol temporal characteristics and its impact on shortwave radiative forcing at a location in the northeast of India, *J. Geophys. Res.*, *115*, D19204, doi:10.1029/2009JD013462.

Rajeev, K., K. Parameswaran, B. V. Thampi, M. K. Mishra, A. K. M. Nair, and S. Meenu (2010), Altitude distribution of aerosols over Southeast Arabian Sea coast during pre-monsoon season: Elevated layers, long-range transport and atmospheric radiative heating, *Atmos. Environ.*, *44*, 2597–2604, doi:10.1016/j.atmosenv.2010.04.014.

Ramanathan, V., et al. (2001a), Indian Ocean Experiment: An integrated analysis of the climate forcing and effects of the great Indo-Asian haze, *J. Geophys. Res.*, *106*, 28,371–28,398, doi:10.1029/2001JD900133.

Ramanathan, V., P. J. Crutzen, J. T. Kiehl, and D. Rosenfeld (2001b), Aerosols, climate, and the hydrological cycle, *Science*, *294*(5549), 2119–2124, doi:10.1126/science.1064034.

Ramanathan, V., M. V. Ramana, G. Roberts, D. Kim, C. Corrigan, C. Chung, and D. Winker (2007), Warming trends in Asia amplified by brown cloud solar absorption, *Nature*, *448*, 575–578, doi:10.1038/nature06019.

Ricchiazzi, P., S. R. Yang, C. Gautier, and D. Sowle (1998), SBDART: A research and teaching software tool for plane-parallel radiative transfer in the Earth's atmosphere, *Bull. Am. Meteorol. Soc.*, *79*(10), 2101–2114, doi:10.1175/1520-0477(1998)079<2101:SARATS>2.0.CO;2.

Rosenfeld, D., Y. Rudich, and R. Lahav (2001), Desert dust suppressing precipitation: A possible desertification feedback loop, *Proc. Natl. Acad. Sci. U. S. A.*, *98*, 5975–5980, doi:10.1073/pnas.101122798.

Rosenfeld, D., U. Lohmann, G. B. Raga, C. D. O'Dowd, M. Kulmala, S. Fuzzi, A. Reissell, and M. O. Andreae (2008), Flood or drought: How do aerosols affect precipitation?, *Science*, *321*, 1309–1313, doi:10.1126/science.1160606.

Sakai, T., T. Shibata, S. A. Kwon, Y. S. Kim, K. Tamura, and Y. Iwasaka (2000), Free tropospheric aerosol backscatter, depolarization ratio, and relative humidity measured with the Raman lidar at Nagoya in 1994–1997: Contributions of aerosols from the Asian continent and the Pacific Ocean, *Atmos. Environ.*, *34*(3), 431–442, doi:10.1016/S1352-2310(99)00328-3.

Schmid, B., J. Michalsky, R. Halthore, M. Beauharnois, L. Harrison, J. Livingston, P. Russell, B. Holben, T. Eck, and A. Smirnov (1999), Comparison of aerosol optical depth from four solar radiometers during the fall 1997 ARM intensive observation period, *Geophys. Res. Lett.*, *26*(17), 2725–2728, doi:10.1029/1999GL900513.

Spinhirne, J. D. (1993), Micro pulse lidar, *IEEE Trans. Geosci. Remote Sens.*, *31*, 48–55, doi:10.1109/36.210443.

Tsai, F., G. T. J. Chen, T. H. Liu, W. D. Lin, and J. Y. Tu (2008), Characterizing the transport pathways of Asian dust, *J. Geophys. Res.*, *113*, D17311, doi:10.1029/2007JD009674.

Twomey, S. (1977), The influence of pollution on the shortwave albedo of clouds, *J. Atmos. Sci.*, *34*, 1149–1152, doi:10.1175/1520-0469(1977)034<1149:TIOPOT>2.0.CO;2.

Wang, S. H., N. H. Lin, M. D. Chou, and J. H. Woo (2007), Estimate of radiative forcing of Asian biomass-burning aerosols during the period of TRACE-P, *J. Geophys. Res.*, *112*, D10222, doi:10.1029/2006JD007564.

Wang, S. H., N. H. Lin, M. D. Chou, S. C. Tsay, E. J. Welton, N. C. Hsu, D. M. Giles, G. R. Liu, and B. N. Holben (2010), Profiling transboundary aerosols over Taiwan and assessing their radiative effects, *J. Geophys. Res.*, *115*, D00K31, doi:10.1029/2009JD013798.

Wang, Z. E., and K. Sassen (2001), Cloud type and macrophysical retrieval using multiple remote sensors, *J. Appl. Meteorol.*, *40*, 1665–1682, doi:10.1175/1520-0450(2001)040<1665:CTAMPR>2.0.CO;2.

Welton, E. J., et al. (2000), Ground-based lidar measurements of aerosols during ACE-2: Instrument description, results, and comparisons with other ground-based and airborne measurements, *Tellus, Ser. B*, *52*, 636–651, doi:10.1034/j.1600-0889.2000.00025.x.

Welton, E. J., K. J. Voss, P. K. Quinn, P. J. Flatau, K. Markowicz, J. R. Campbell, J. D. Spinhirne, H. R. Gordon, and J. E. Johnson (2002), Measurements of aerosol vertical profiles and optical properties during INDOEX 1999 using micro-pulse lidars, *J. Geophys. Res.*, *107*(D19), 8019, doi:10.1029/2000JD000038.

Xia, X., Z. Li, B. Holben, P. Wang, T. Eck, H. Chen, M. Cribb, and Y. Zhao (2007), Aerosol optical properties and radiative effects in the Yangtze Delta region of China, *J. Geophys. Res.*, *112*, D22S12, doi:10.1029/2007JD008859.

Xu, J., M. H. Bergin, X. Yu, G. Liu, J. Zhao, C. M. Carrico, and K. Baumann (2002), Measurement of aerosol chemical, physical and radiative properties in the Yangtze delta region of China, *Atmos. Environ.*, *36*(2), 161–173, doi:10.1016/S1352-2310(01)00455-1.

Yu, H., et al. (2006), A review of measurement-based assessments of aerosol direct radiative effect and forcing, *Atmos. Chem. Phys.*, *6*, 613–666, doi:10.5194/acp-6-613-2006.

Yu, H., et al. (2009), Remote sensing and in-situ measurements of aerosol properties, burdens, and radiative forcing, in *Atmospheric Aerosol Properties and Climate Impacts: Synthesis and Assessment Product 2.3: Report by the U.S. Climate Change Science Program and the Subcommittee on Global Change Research*, edited by M. Chi, R. A. Kahn, and S. E. Schwartz, pp. 21–54, U.S. Clim. Change Sci. Program, Washington, D. C.

Yu, X., B. Zhu, and M. Zhang (2009), Seasonal variability of aerosol optical properties over Beijing, *Atmos. Environ.*, *43*(26), 4095–4101, doi:10.1016/j.atmosenv.2009.03.061.

Zhou, J., G. Yu, C. Jin, F. Qi, D. Liu, H. Hu, Z. Gong, G. Shi, T. Nakajima, and T. Takamura (2002), Lidar observations of Asian dust over Hefei, China, in spring 2000, *J. Geophys. Res.*, *107*(D15), 4252, doi:10.1029/2001JD000802.

M. Cribb and Z. Li, Earth System Science Interdisciplinary Center, University of Maryland, 5825 University Research Ct., Ste. 4001, College Park, MD 20742–3823, USA. (zli@atmos.umd.edu)

C. Flynn, Climate Physics Group, Pacific Northwest National Laboratory, MS K9-24, PO Box 999, Richland, WA 99352, USA.

J. Liu and Y. Zheng, Jiangsu Key Laboratory of Atmospheric Environment Monitoring and Pollution Control, Nanjing University of Information Science and Technology, Nanjing 210044, China.